

PROTOSTAR FORMATION IN MAGNETIC MOLECULAR CLOUDS BEYOND ION DETACHMENT: III. A PARAMETER STUDY

KONSTANTINOS TASSIS^{1,2} & TELEMACHOS CH. MOUSCHOVIAS¹

Draft version October 30, 2018

ABSTRACT

In two previous papers we formulated and solved, for a fiducial set of free parameters, the problem of the formation and evolution of a magnetically supercritical core inside a magnetically subcritical parent cloud. The evolution was followed into the opaque phase that resulted in the formation of a hydrostatic protostellar core. In this paper we present a parameter study to assess the sensitivity of the results (1) to the density at which the equation of state becomes adiabatic; (2) to the initial mass-to-flux ratio of the parent cloud; and (3) to ionization by radioactive decay of different nuclei (⁴⁰K and ²⁶Al) at high densities ($n_n \gtrsim 10^{12} \text{ cm}^{-3}$). We find that (1) the results depend only slightly on the density at which the onset of adiabaticity occurs; (2) memory of the initial mass-to-flux ratio is completely lost at late times; and (3) the precise source of radioactive ionization alters the degree of attachment of the electrons to the field lines (at high densities), and the relative importance of ambipolar diffusion and Ohmic dissipation in reducing the magnetic flux of the protostar. The value of the magnetic field at the end of the runs is insensitive to the values of the free parameters and in excellent agreement with meteoritic measurements of the protosolar nebula magnetic field. The magnetic flux problem of star formation is resolved for at least strongly magnetic newborn stars. A complete detachment of the magnetic field from the matter is unlikely. The formation of a “magnetic wall” (with an associated magnetic shock) is independent of the assumed equation of state, although the process is enhanced and accelerated by the formation of a central hydrostatic core.

Subject headings: ISM: clouds – ISM: dust – magnetic fields – MHD – stars: formation – shock waves

1. INTRODUCTION

We previously formulated the problem of the ambipolar-diffusion-initiated core formation and evolution in self-gravitating, magnetically supported model clouds (Tassis & Mouschovias 2006a, hereafter Paper I), and presented the solution for a typical model cloud (Tassis & Mouschovias 2006b, hereafter Paper II). In this paper, we quantify the dependence of the results on the values of the relevant free parameters of the problem.

The system of MHD equations governing the evolution of the model cloud, which we presented in Paper I, contains four free parameters: the dimensionless initial central mass-to-flux ratio $\mu_{d,c0}$ of the reference state relative to its critical value for collapse; the characteristic lengthscale \tilde{l}_{ref} of the initial column density distribution relative to the thermal critical lengthscale; the ratio of the external thermal pressure and “gravitational pressure” in the central flux tube of the initial reference state, \tilde{P}_{ext} ; and the density at which the transition from an isothermal to an adiabatic equation of state occurs, n_{opq} . Additional parameters involved in the chemical model are well constrained observationally and experimentally (see Appendix in Desch & Mouschovias 2001 and references therein), and values from these studies are used in the calculations.

Of the parameters referred to above, the value of \tilde{P}_{ext} has no significant effect on the formation and evolution

of the supercritical core in a *self-gravitating* model cloud. The value of \tilde{l}_{ref} is a measure of the strength of the initial thermal-pressure forces relative to gravitational forces inside the model cloud. If $\tilde{l}_{\text{ref}} > 3\sqrt{2}$ then the cloud is thermally supercritical. Basu & Mouschovias (1995) showed that, as long as the cloud is significantly thermally supercritical, the value of \tilde{l}_{ref} plays no role other than to determine the size and hence the mass of the initial cloud (which they found to be proportional to \tilde{l}_{ref}^2). Hence, the effect of varying \tilde{P}_{ext} and \tilde{l}_{ref} is not examined further in this parameter study. The values used for these parameters in all the models presented in this paper are $\tilde{P}_{\text{ext}} = 0.1$ and $\tilde{l}_{\text{ref}} = 5.5\pi = 4.07 \times (3\sqrt{2})$.

The free parameters varied are the density at which the equation of state becomes adiabatic, n_{opq} , and the initial mass-to-flux ratio of the parent cloud μ_d in units of the critical value. We also examine how the results change when, at high densities (when natural radioactivity dominates cosmic rays as the primary ionization mechanism), radioactive ²⁶Al rather than ⁴⁰K is the most abundant decaying element.

Table 1 shows the relevant parameters of the models studied in this paper. Model *f* is our fiducial run that was presented in Paper II. In § 2 we examine how the results of the calculations change as the density n_{opq} , at which the transition from isothermality to adiabaticity occurs, is varied. For this purpose, we compare results from three models: *n10*, *f* and *n12*, in which all parameters have the same values as in the fiducial run, except n_{opq} ; it is equal to 10^{10} , 10^{11} and 10^{12} cm^{-3} in the three models, respectively. These values cover the expected density range in which the collapsing core

¹ Departments of Physics and Astronomy, University of Illinois at Urbana-Champaign, 1002 W. Green Street, Urbana, IL 61801

² Department of Astronomy and Astrophysics and the Kavli Institute for Cosmological Physics, The University of Chicago, 5640 South Ellis Avenue Chicago, IL 60637

TABLE 1
MODEL PARAMETERS

Model	$n_{\text{opq}} (\text{cm}^{-3})$	$\mu_{\text{d},\text{c}0}$	dominant radionuclide
<i>f</i>	10^{11}	0.25	^{40}K
<i>n10</i>	10^{10}	0.25	^{40}K
<i>n12</i>	10^{12}	0.25	^{40}K
<i>i</i>	always isothermal	0.25	^{40}K
<i>m5</i>	10^{11}	0.50	^{40}K
<i>m7</i>	10^{11}	0.70	^{40}K
<i>m9</i>	10^{11}	0.90	^{40}K
<i>Al</i>	10^{11}	0.90	^{26}Al

will become optically thick (Gaustad 1963; Hayashi 1966; Draine & Lee 1984; Ossenkopf & Henning 1994; Masunaga & Inutsuka 1999). As part of this parameter study, we also present in § 2.1 results for model *i*, a “control run”, in which the isothermal approximation is retained throughout the calculation. Although clearly unrealistic, this run is used to assess which effects are caused by the change in the equation of state. The effect of the initial mass-to-flux ratio on the solution is discussed in § 3. We present results for four models, *f*, *m5*, *m7* and *m9*, with parameters always the same as those of the fiducial run, except $\mu_{\text{d},\text{c}0}$, which is equal to 0.25, 0.5, 0.7 and 0.9, respectively. Finally, in § 4 we examine how the (late-time) results depend on the kind of radioactive element that dominates the ionization process at high densities. If the mass-to-flux ratio of the parent cloud is close to critical, then the evolution is much more rapid than in the fiducial model, and radionuclides with half-lives shorter than ^{40}K may contribute significantly to the ionization at high densities. For this reason, we compare models *m9* and *Al*, both of which have $\mu_{\text{d},\text{c}0} = 0.9$, but assume different dominant radionuclides (^{40}K and ^{26}Al , respectively).

2. DEPENDENCE ON N_{OPQ}

In this section we examine the effect of varying the density at which the assumed equation of state changes from isothermal to adiabatic. We compare three models: *n10* ($n_{\text{opq}} = 10^{10} \text{ cm}^{-3}$); *f* ($n_{\text{opq}} = 10^{11} \text{ cm}^{-3}$); and *n12* ($n_{\text{opq}} = 10^{12} \text{ cm}^{-3}$). Model *f* is the fiducial run, which was discussed in detail in Paper II. All three models have an initial mass-to-flux ratio $\mu_{\text{d},\text{c}0} = 0.25$.

Figure (1) exhibits central quantities of the model clouds as functions of the central number density of neutrals. In all cases, the solid line corresponds to model *f*, while the dashed and dashed-dot lines correspond to models *n10* and *n12*, respectively.

Figure (1a) shows the central temperature (measured in K) of the three models as a function of the central neutral density. At low densities, while the equation of state is still isothermal, the central temperature remains constant and equal to the 10 K temperature of the reference state. In each model, at a density equal to n_{opq} , the equation of state becomes adiabatic and the temperature begins to deviate from its initial value. The evolution of temperature follows the adiabatic law, $T \propto \rho^{\gamma-1}$. The break in the power law and the subsequent, less steep increase, is the result of the excitation of the rotational degrees of freedom of the neutral molecules, which corresponds to a shift in the adiabatic index from 5/3 to

7/5. In the models we implement this change at a temperature of 200 K. The models do not all reach the same central density when each run is stopped. This is because the termination criterion for each run is that the central temperature reaches 1000 K, at which thermal ionization (not accounted for in the model) is expected to become important. This temperature is reached at a different central density in each model (6×10^{13} , 6×10^{14} , and $6 \times 10^{15} \text{ cm}^{-3}$ in models *n10*, *f*, and *n12*, respectively), depending only on the value of n_{opq} .

Figure (1b) displays the dependence of the central mass-to-flux ratio, normalized to its critical value, on the central density of neutrals. The behavior in all cases is very similar to that of the fiducial run (model *f*). The three curves deviate slightly from one another close to the density n_{opq} of each model, while they quickly asymptote to an identical behavior at higher $n_{\text{n},\text{c}}$. This is because B_z exhibits only a mild dependence on the n_{opq} at high densities.

The evolution of the central magnetic field with density (both z - and r - components, shown in Figs. 1c and 1d, respectively) exhibits a relatively weak dependence on n_{opq} . The most pronounced difference is caused by a steepening of the density dependence of $B_{z,\text{c}}$ immediately after the onset of adiabaticity. If the equation of state had remained isothermal, $B_{z,\text{c}}$ would have turned over and would have asymptoted to a constant value at high densities (see Fig. 7c below). The behavior of $B_{z,\text{c}}$ is similar in all three models *after* the onset of adiabaticity. However, in model *n12* the overall value of $B_{z,\text{c}}$ is smaller at a given density than that in models *n10* and *f*. This is so because in model *n12*, adiabaticity is turned on at a density greater than that at which the profile of $B_{z,\text{c}}$ begins to flatten, while in the other two models adiabaticity is turned on at a density smaller or about equal to that at which the flattening would begin. Despite this fact, all runs end at a similar value of $B_{z,\text{c}} \approx 10^5 \mu\text{G}$, because the final central density of each model increases with n_{opq} .

The r -component of the magnetic field at the center of the contracting core $B_{r,\text{c}}$ reaches a maximum at a density $n_{\text{n},\text{c}} \approx 10^{11} \text{ cm}^{-3}$ and decreases beyond that. This is because at that density the magnetic field begins to decouple from the matter and the field-line deformation can no longer be sustained.

Figure (2) shows the radial dependence of the density of the neutrals, n_{n} , of its logarithmic derivative, $s = d \ln n_{\text{n}} / dr$, and of the temperature, T , at different times. The top, middle and bottom rows refer to models *n10*, *f*, and *n12*, respectively. Each curve corresponds to a central density enhancement of one order of magnitude with respect to the previous curve, except for the last curve, which always corresponds to a central temperature of 1000 K. The “star” on a curve marks the location of the supercritical core boundary.

The rightmost column of Figure 2 shows profiles of the temperature. Only the five last curves in each case show deviation from the reference-state temperature. The radius at which adiabaticity sets in does not change appreciably with time. This is so because adiabaticity is implemented using a number-density criterion, and does not change in time (see left column plots). This radius is somewhat closer to the center the greater n_{opq} is, because

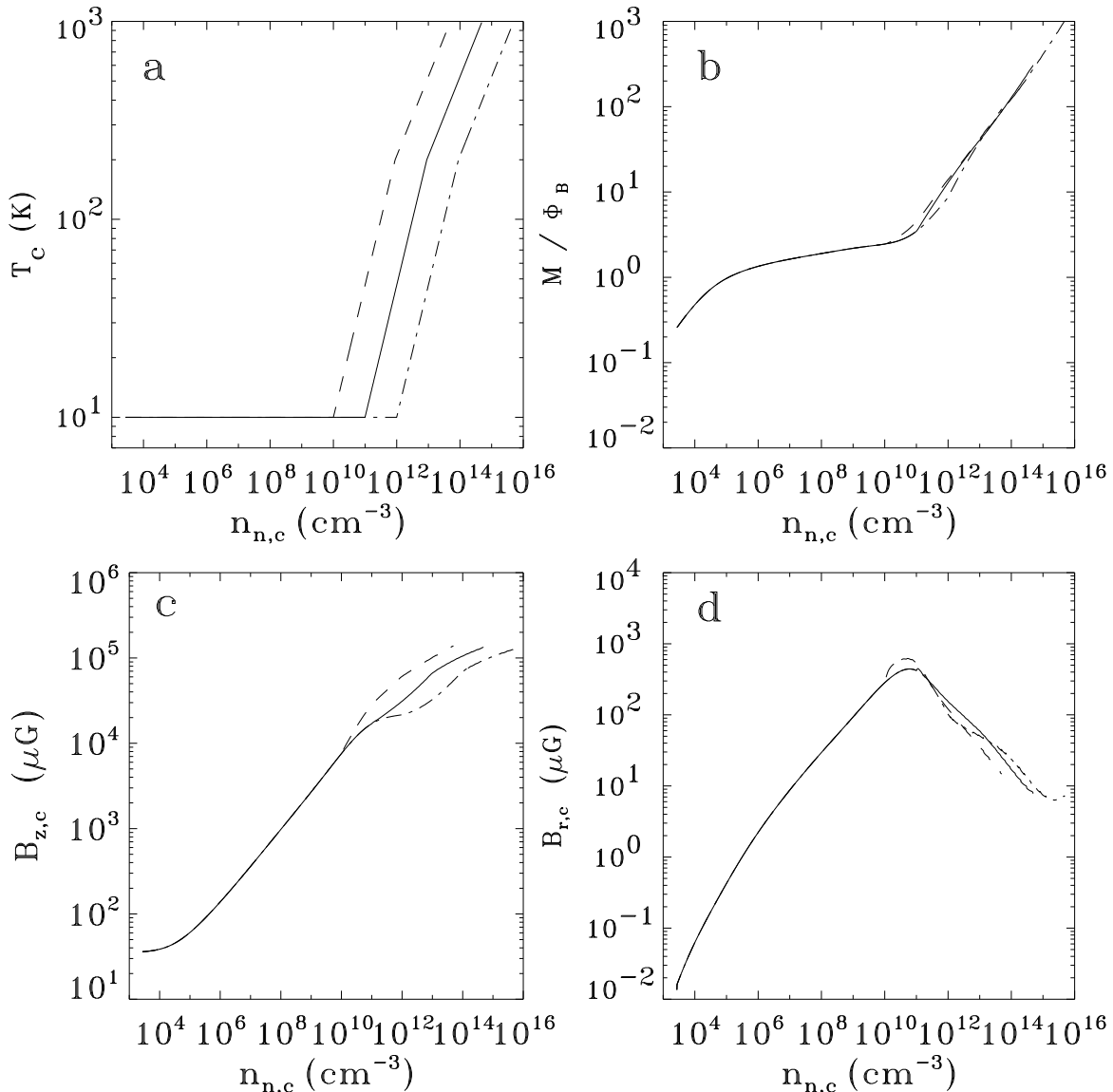


FIG. 1.— Central quantities as functions of the central number density of neutrals (in cm^{-3}) for models *f* (solid line, $n_{\text{opq}} = 10^{11} \text{cm}^{-3}$), *n10* (dashed line, $n_{\text{opq}} = 10^{10} \text{cm}^{-3}$), and *n12* (dashed-dot line, $n_{\text{opq}} = 10^{12} \text{cm}^{-3}$). (a) Central temperature (in K); (b) central mass-to-flux ratio normalized to the critical value; (c) z -component of the magnetic field (in μG) at the center; (d) r -component of the magnetic field (in μG) at the center.

the density decreases monotonically with r . The qualitative behavior of the number density of the neutrals (left column) is the same as that discussed in Paper II (Fig. 3c) for the fiducial run, with the power-law density profile steepening after the onset of adiabaticity. The final central density achieved by the time the temperature of 1000 K has been reached increases with the value of n_{opq} , and is therefore greatest in model *n12*.

In Paper II (Fig. 3d) we discussed the qualitative behavior of the logarithmic slope of the number density s and pointed out that the two innermost dips are of thermal and magnetic origin, with the inner dip corresponding to a balance between the thermal-pressure and gravitational forces, and the outer dip corresponding to a balance between magnetic and gravitational forces. The overall magnitude of the thermal dip is essentially unchanged for different values of n_{opq} . However, its location moves inward for greater n_{opq} as all of the post-

adiabaticity features are translated toward smaller radii. By contrast, the amplitude of the magnetic dip does change with n_{opq} ; it is greater for smaller n_{opq} .

Figure 3 shows radial profiles of the z -component of the magnetic field (left column) and of its spatial derivative, $b = d \ln B_z / d \ln r$ (right column). All models exhibit similar behavior. There is a flat inner region followed by a local maximum at the boundary of the hydrostatic core. Just outside, the magnetic field decreases rapidly and the profile becomes steeper because the transition to adiabaticity occurs at smaller densities. In the isothermal regime there is a more gradual decrease with radius (mean slope ≈ -0.7) out to the boundary of the supercritical core. The profile of the magnetic field at the cloud envelope is not affected by the evolution of the supercritical core. Finally, the break in b moves from $r/R_0 \approx 2 \times 10^{-5}$ in model *n10* to $r/R_0 \approx 8 \times 10^{-6}$ in model *n12*, and the maximum value

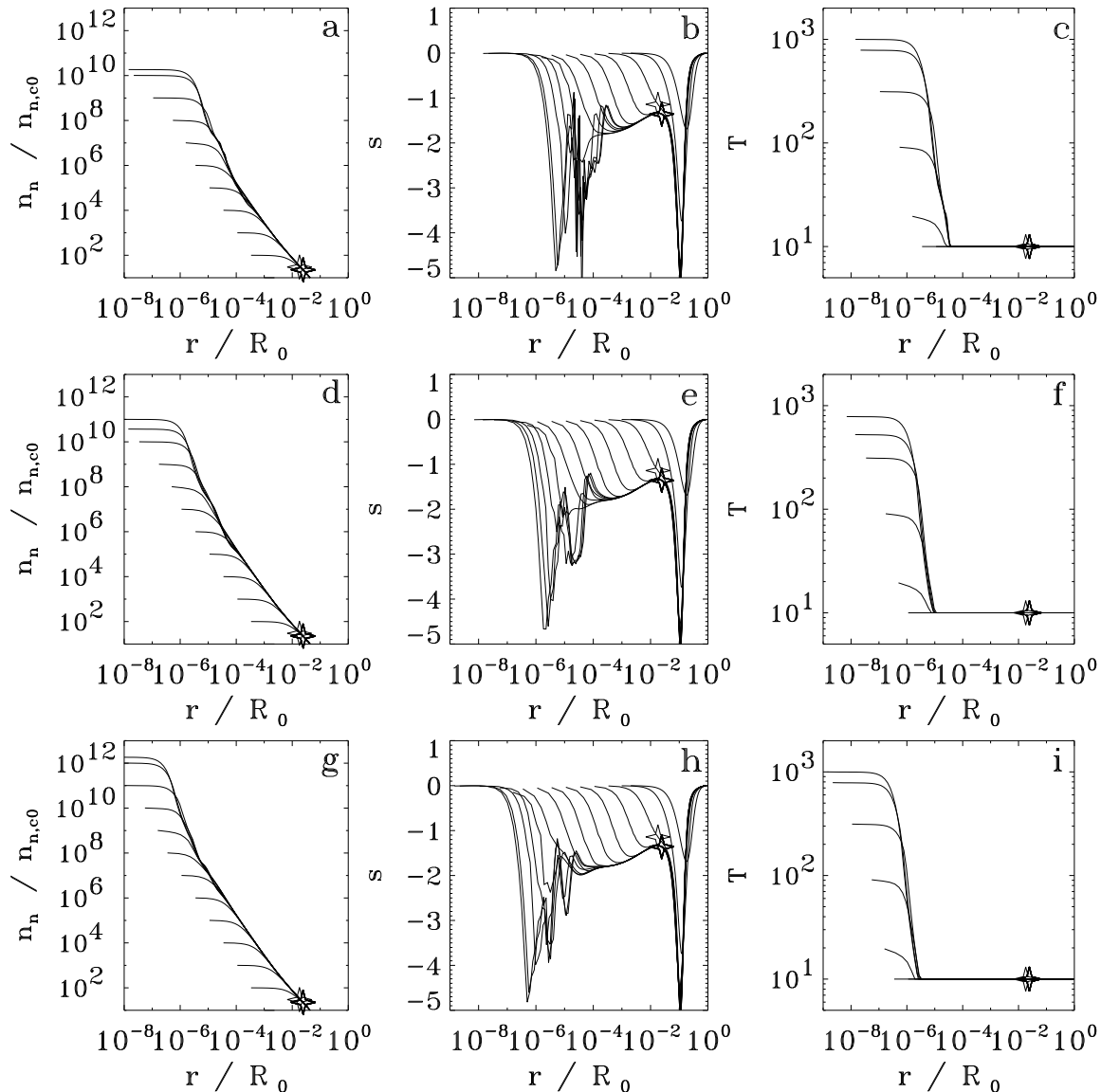


FIG. 2.— Radial profiles, at different times, for models *n10* (top row, $n_{\text{opq}} = 10^{10} \text{ cm}^{-3}$), *f* (middle row, $n_{\text{opq}} = 10^{11} \text{ cm}^{-3}$), and *n12* (bottom row, $n_{\text{opq}} = 10^{12} \text{ cm}^{-3}$). The times are chosen such that neighboring curves differ by a factor of 10 in central neutral density. *Left column*: central number density of neutrals normalized to its initial value in the initial equilibrium state ($n_{n,c0} = 2711 \text{ cm}^{-3}$); *middle column*: spatial derivative of the density $s = d \ln n_n / d \ln r$; *right column*: temperature (in K).

of B_z from $r/R_0 \approx 10^{-5}$ in model *n10* to $r/R_0 \approx 5 \times 10^{-6}$ in model *n12*.

Figure 4 exhibits radial profiles of the ratio of thermal-pressure and gravitational forces (left column) and magnetic and gravitational force (right column) at different times. Each curve corresponds to a central density enhancement of one order of magnitude with respect to the previous curve, except for the last curve, which always corresponds to a central temperature of 1000K. The thermal-pressure force becomes comparable to the gravitational force in the opaque core only after the onset of adiabaticity. The location of the thermal shock coincides with the hydrostatic core boundary. Because the density decreases monotonically with radius and the extent of the opaque region is limited by the condition $n \geq n_{\text{opq}}$, the size of the hydrostatic core decreases with increasing n_{opq} .

The ratio of magnetic and gravitational forces ex-

hibits the local maximum discussed in Paper II, which is the cause of the magnetic shock, and the corresponding magnetic feature in the density profile. As n_{opq} increases, the location of this maximum is displaced toward smaller radii, and the ratio F_M/F_G in the hydrostatic core reaches smaller values. This is so because, as n_{opq} increases, the transition from isothermality to adiabaticity takes place at higher densities and the termination condition for each run ($T = 1000 \text{ K}$) is achieved at greater central densities.

The small-amplitude oscillations which appear in the ratio of magnetic and gravitational forces inside the hydrostatic core are numerical noise due to the unavoidable inaccuracies involved in calculating spatial derivatives (needed to derive the magnetic force) inside the hydrostatic core, where the magnetic field is very nearly spatially uniform. However, because in this region the magnetic field is dynamically unimportant, the impact of

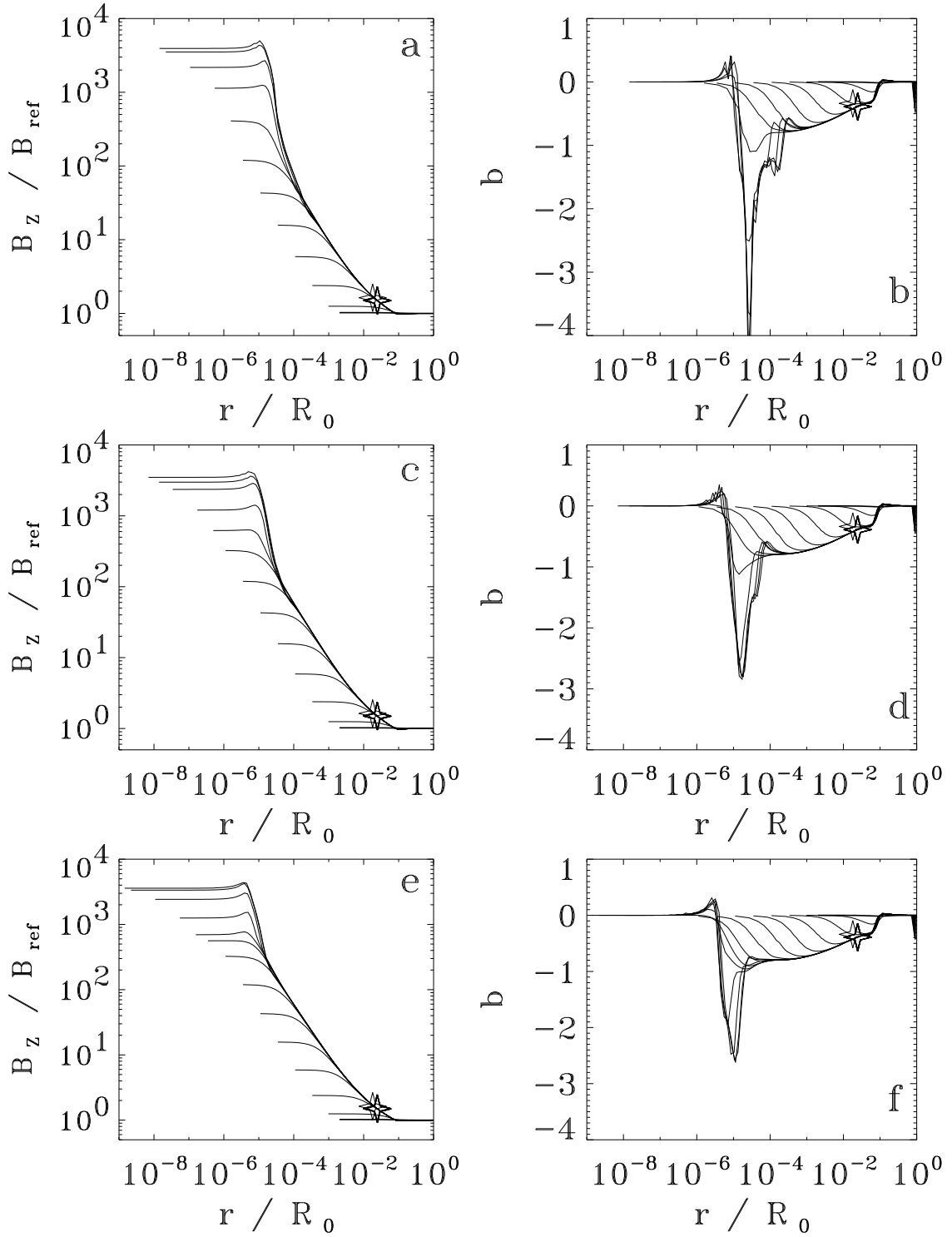


FIG. 3.— Radial profiles of the z -component of the magnetic field, normalized to the field strength of the reference state (left column), and of its spatial derivative, $b = d \ln B_z / d \ln r$ (right column) at different times, as in Figure (2). *Top row*: model $n10$; *middle row*: model $n12$; *bottom row*: model $n12$.

such noise on our results is insignificant. The disconnected line in panel (f) is due to logarithmic plotting (in the region where the line has not been plotted, the value of the magnetic force has become numerically zero).

Figure 5 shows the spatial profiles of the radial velocities of the neutrals (left column) and the electrons (right column) in units of the sound speed (in the neutrals) of the reference state, for the three models $n10$, f and $n12$ (top to bottom row). All models exhibit the same qualitative behavior: There are always two features in the velocity of the neutrals, the “thermal” shock and the “magnetic” shock at somewhat greater radii. The velocity of the electrons (which are, except at very small radii in model $n12$, well attached to the magnetic field) exhibits only the magnetic

shock. Its effect is much more pronounced than in the case of the neutrals, and the electrons decelerate almost to a halt, at the boundary of the hydrostatic core.

The positions of the magnetic and the thermal shocks move to smaller radii with increasing n_{opq} , because the boundary of the hydrostatic core (which moves inward with increasing n_{opq}) determines the position of the thermal shock and, by extension, the position of the magnetic feature, which is caused by field lines piling up *just outside* the hydrostatic core. The maximum infall velocity of both neutrals and electrons increases somewhat as n_{opq} increases, because the delay of the onset of adiabaticity implies accelerated infall for longer times. In addition, the reacceleration of the neutrals between the magnetic and the thermal shocks is greater with increasing n_{opq} . This is because, as seen in Figure 4, in the case of smaller n_{opq} the thermal-pressure force as a fraction of the gravitational force increases faster with decreasing radius between the magnetic shock and the hydrostatic core, and hence the reacceleration is milder.

The left column of Figure 6 provides crucial information concerning the importance of the magnetic field during the late stages of star formation and whether a complete detachment of the field from the matter can occur before thermal ionization reattaches matter to the field lines at $T \approx 1000$ K. At the late stages of contraction of the supercritical core, which are for the first time followed in this series of papers, ions have detached from the magnetic field lines and follow the motion of the neutrals. Hence, the electrons are the only particles that may remain attached to the field lines until the onset of thermal reionization of the core. The degree of attachment of electrons to the field lines is measured, as we have discussed in Papers I and II, by the attachment parameter Δ_e . The value $\Delta_e \approx 1$ indicates that the electrons are well coupled to the field lines, while $\Delta_e \approx 0$ indicates that the electrons have detached and follow the motion of the neutrals.

As seen in the left-column plots of Figure 6, in the model with $n_{\text{opq}} = 10^{10} \text{ cm}^{-3}$, the electrons remain well attached to the magnetic field throughout the run. In the case $n_{\text{opq}} = 10^{11} \text{ cm}^{-3}$, the electrons begin to detach before the central temperature reaches 1000 K, at which the run is stopped. However, their degree of attachment is still high. Finally, in the model with $n_{\text{opq}} = 10^{12} \text{ cm}^{-3}$, the electrons in the core have detached almost completely before the end of the run ($\Delta_e \approx 0.1$).

Using the indirect attachment parameter of the electrons to trace the densities at which the electron de-

tachment begins and comes to completion, we find that electrons begin to detach at about 10^{14} cm^{-3} and detach completely by a density $\approx 10^{16} \text{ cm}^{-3}$, regardless of the value of n_{opq} . Hence, we arrive at the conclusion that *the detachment of electrons (and consequently the complete decoupling of matter) from the magnetic field lines takes place at a number density $\approx 10^{15} \text{ cm}^{-3}$, provided that this density can be reached before thermal ionization becomes important.* In order to confidently assert whether the required density is achieved before thermal ionization sets in, and hence whether this complete decoupling of matter from the magnetic field occurs in nature, the temperature history of the collapsing core would need to be followed in detail, accounting for radiative transfer. However, given the results of our parameter study, the detachment of electrons before the onset of thermal ionization is unlikely. This is so because the actual temperature will increase more by the time the central density becomes 10^{15} cm^{-3} than it does in the isothermal approximation up to 10^{12} cm^{-3} , beyond which adiabaticity was assumed.

A second important issue during the very late stages of collapse is whether and when Ohmic dissipation overtakes ambipolar diffusion as the dominant flux reduction mechanism. This issue is explored by the right-column plots of Figure 6, which show radial profiles of the ratio of the ambipolar-diffusion and Ohmic-dissipation timescales. The ambipolar-diffusion timescale is smaller at all radii and times, except in the very late stages of the contraction, at densities $\gtrsim 10^{13} \text{ cm}^{-3}$. For densities $\sim 10^{16} \text{ cm}^{-3}$, the Ohmic-dissipation timescale becomes ≈ 100 times smaller than the corresponding ambipolar-diffusion timescale. *Thus the density at which Ohmic dissipation becomes more effective than ambipolar diffusion is not sensitive to the thermal history of the protostellar core, but the size of the region in which this happens is: The greater the density at which the protostellar core becomes opaque, the smaller the region in which Ohmic dissipation dominates.*

2.1. The Isothermal Control Run

In this section we present results of a “control run” for which the assumption of isothermality is retained throughout the evolution of the contracting model cloud. These results complement the parameter study with regard to n_{opq} , by allowing one to identify the features that can be attributed to the transition between equations of state. All parameters other than the equation of state are identical with those of the runs discussed in the previous section.

Figure (7) shows the evolution of central quantities for this model. The dependence of the central density of neutral particles on time is plotted in Figure (7a). This curve is essentially identical to the corresponding one of the fiducial run discussed in Paper II, since the slow, ambipolar-diffusion-controlled early stage of the formation of the supercritical core occurs isothermally in both models.

The evolution of the central mass-to-flux ratio and of the r -component of the magnetic field at the center of the cloud, shown in Figures (7b) and (7d), respectively, remained essentially the same for different values of n_{opq} , as we saw in the previous section. It is also very similar in the isothermal run. However, the evolution of the z -

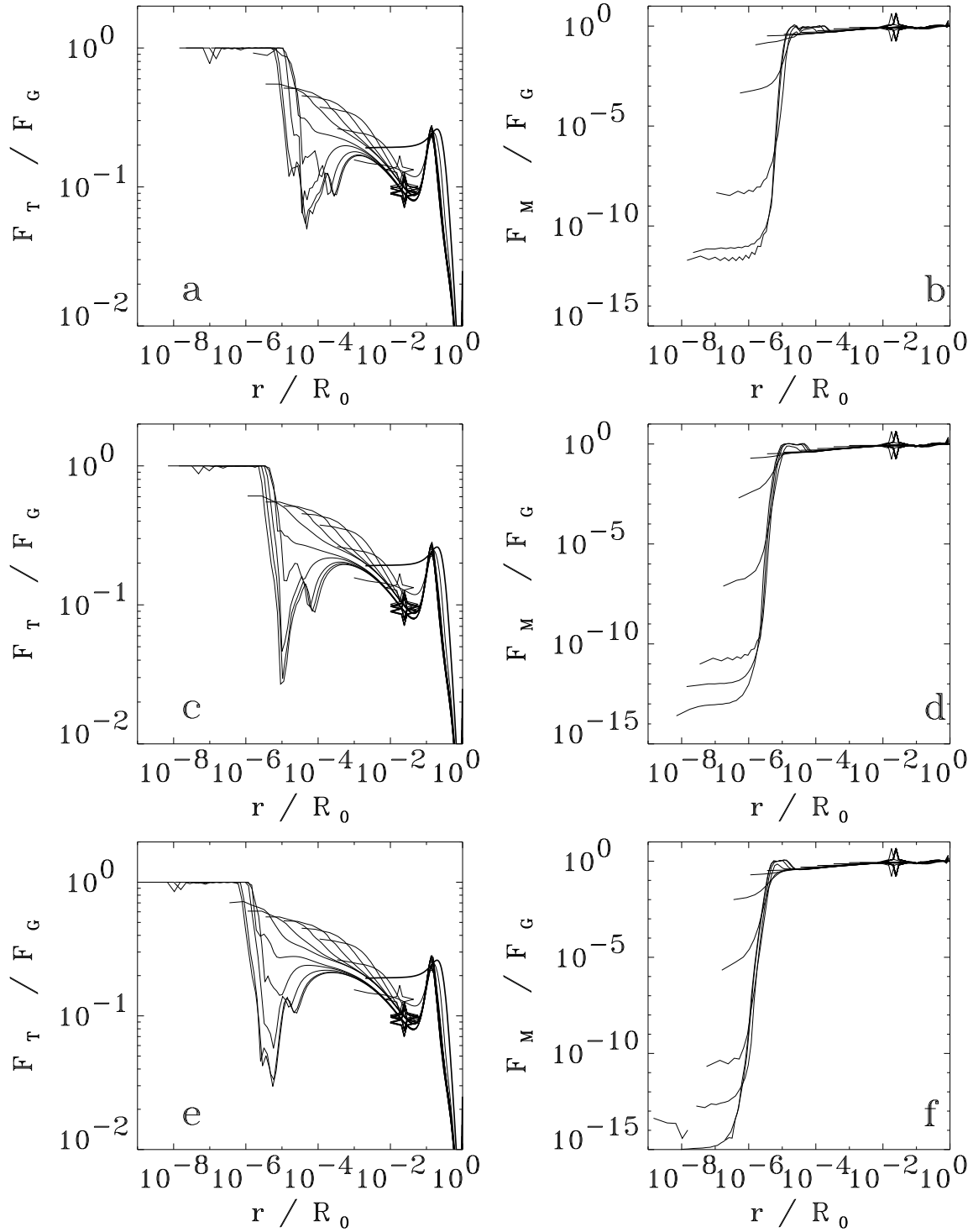


FIG. 4.— Radial profiles of the ratio of thermal-pressure and gravitational forces (left column), and magnetic and gravitational forces (right column) at different times, chosen as in Figure (2). *Top row*: model $n10$; *middle row*: model f ; *bottom row*: model $n12$. The “star” marks the location of the supercritical core boundary.

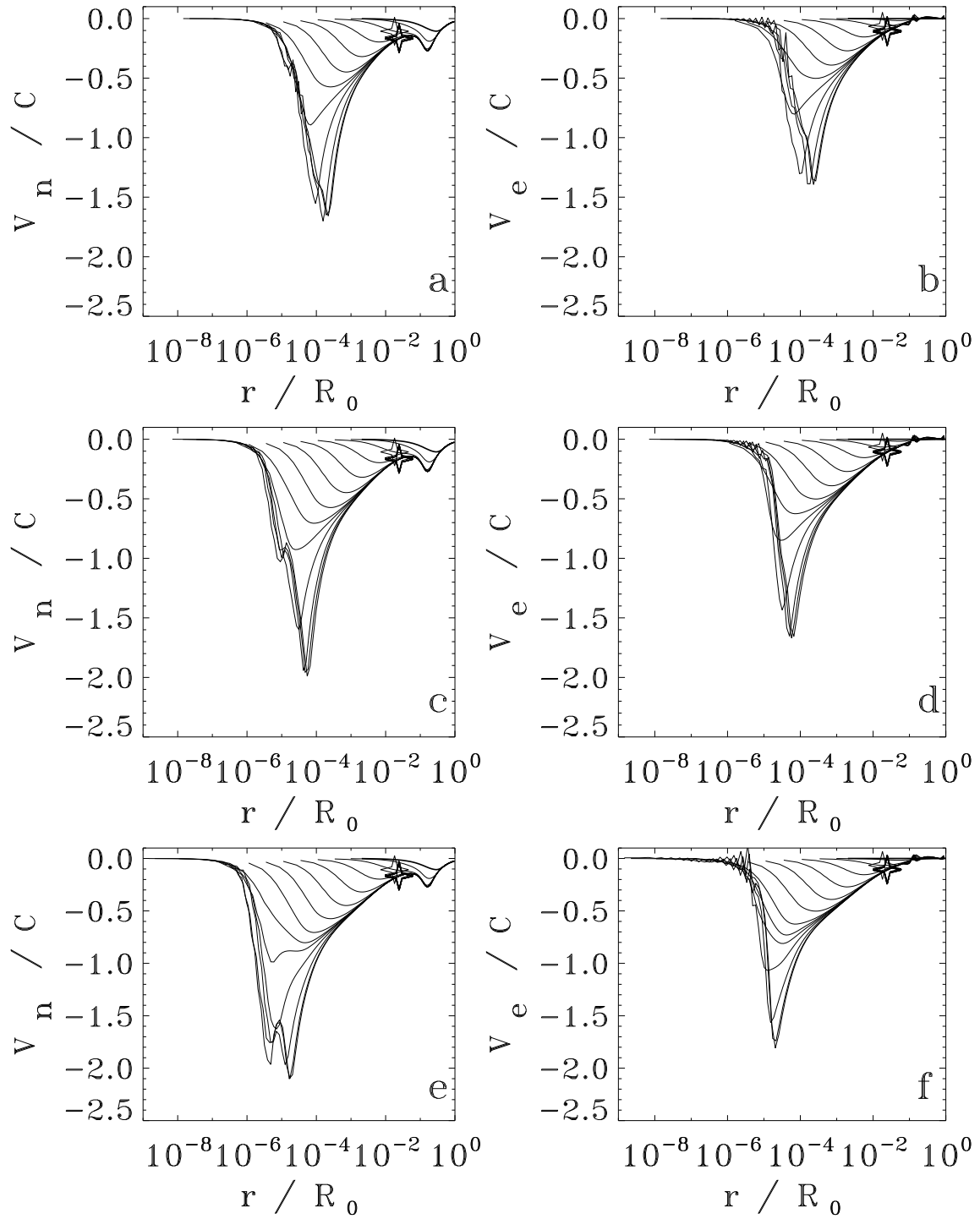


FIG. 5.— Spatial profiles of the radial velocities of the neutrals (left column) and the electrons (right column), normalized to the sound speed of the reference state, at different times chosen as in Figure (2). *Top row:* model n10; *middle row:* model f; *bottom row:* model n12. The “star” marks the location of the supercritical core boundary.

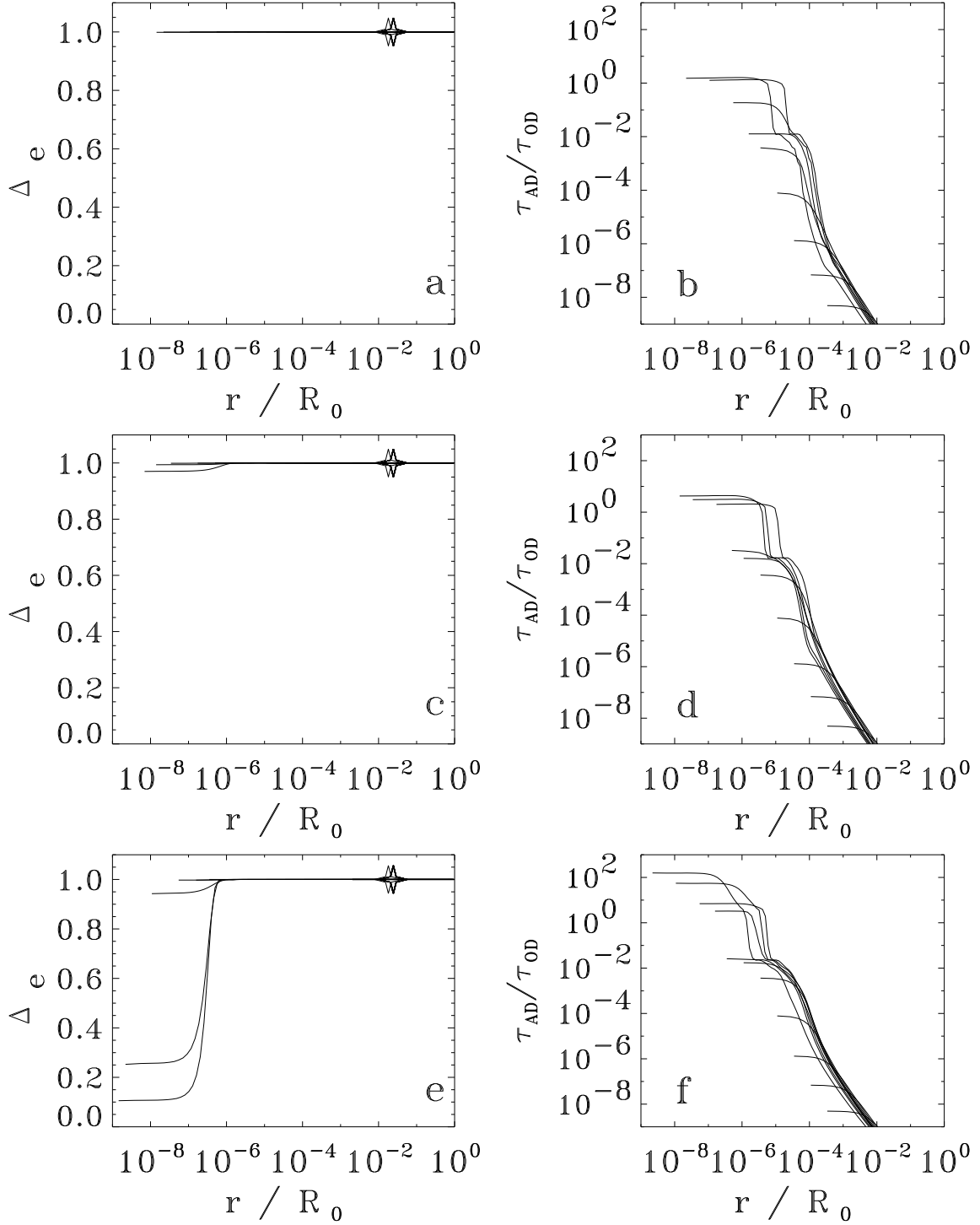


FIG. 6.— Radial profiles of the attachment parameter of the electrons (left column) and the ratio of ambipolar-diffusion and Ohmic-dissipation timescales (right column) at different times, chosen as in Figure (2). *Top row:* model n10; *middle row:* model f; *bottom row:* model n12. The “star” marks the location of the supercritical core boundary.

component of the magnetic field, shown in Figure (7c), shows a qualitatively different behavior at late times. In the previous section it was shown that, after adiabaticity sets in, the dependence of $B_{z,c}$ on density steepens, and $B_{z,c}$ keeps increasing until the end of the run. In the isothermal model, this steepening never takes place. Instead, the curve flattens and $B_{z,c}$ asymptotically approaches 0.28 G, a value which is about 800 times the magnetic field of the initial reference state, and slightly greater than the one reached in the adiabatic runs by the time the temperature became 1000 K.

Figures (8c) and (8d) show the neutral number density profile and its derivative, $s = d \ln n_n / d \ln r$, respectively, at different times chosen as in Figure (2). As before, each curve corresponds to an order of magnitude enhancement in the central density relative to the previous curve. In § 2, (in relation to Fig. 2) and in Paper II, we identified two types of features inside the supercritical core but outside the innermost uniform-density region in the density profile and its derivative: an inner, “thermal” steepening of the profile, corresponding to a dip in the slope s , and a second, “magnetic” steepening, due to the local maximum in the z -component of the magnetic field and the corresponding balance between magnetic and gravitational forces. In the isothermal run, the inner thermal feature is completely absent, because the temperature remains always at 10 K and a hydrostatic core never forms. The magnetic feature is still present, but is less pronounced because the enhanced “pile-up” of matter and magnetic flux outside the hydrostatic core is now absent.

Spatial profiles of the velocities of the neutral molecules and the field lines are shown in Figure (8a) and (8b), respectively. Again, only the magnetic feature is present here, at $r = 10^{-5} R_0$, and it is much weaker than the corresponding magnetic shocks seen in the runs that allow adiabaticity at the highest densities. The reason for this difference is that the presence of the hydrostatic core leads to a more pronounced accumulation of flux just outside its boundary.

Figures (8e) and (8f) display spatial profiles of B_z and its logarithmic derivative, b , at different times as in Figure (2). Although the qualitative behavior of B_z is similar to that of the models discussed above (moving from larger to smaller radii, a steepening of the power-law profile, followed by a local maximum and then the innermost flat region), all features are less pronounced in the present, isothermal case. This is especially evident in the case of the local maximum, because of the “pile-up” of field lines and matter that occurs just outside the hydrostatic core in the adiabatic case.

Figures (9a) and (9b) show the spatial variation of the ratios of thermal-pressure and gravitational forces, and magnetic and gravitational forces, respectively. In the isothermal model, the thermal-pressure force never balances the gravitational force. However, in the innermost part of the collapsing supercritical core at late times, the thermal-pressure force overtakes the magnetic force. In this region, then, at late times, the thermal-pressure forces provide the main opposition to gravity even in this isothermal run.

The spatial variation of the attachment parameter of the electrons, Δ_e , is shown in Figure (9c) at different times, as in Figure (2). As discussed above, the detach-

ment of the electrons is primarily density related. The electrons are completely detached from the field lines by $n_n \approx 10^{16} \text{ cm}^{-3}$.

The ratio of the ambipolar-diffusion and Ohmic-dissipation timescales is shown in Figure 9d as function of radius, normalized as usual to the initial cloud radius R_0 , at different times. Below $n_{n,c} \approx 10^{14} \text{ cm}^{-3}$, ambipolar diffusion is much more effective than Ohmic dissipation in increasing the mass-to-flux ratio in any given flux tube. It is only for densities greater than $\approx 10^{14} \text{ cm}^{-3}$ that Ohmic dissipation becomes more important than ambipolar diffusion. This density is slightly greater than in the adiabatic cases.

Having examined the limiting isothermal case, we conclude that the results concerning the structure of the magnetic field, the evolution of the ratio of ambipolar-diffusion and Ohmic-dissipation timescales, and the density at which the electrons detach from the magnetic field, are not sensitive to the assumed equation of state. However, the presence of a hydrostatic core in the adiabatic models accelerates the formation of the “magnetic wall” (the evolution of which eventually leads to the series of magnetically driven shocks studied in Tassis & Mouschovias 2005a,b).

3. DEPENDENCE ON THE MASS-TO-FLUX RATIO

In order to quantify the effect of the initial mass-to-flux ratio of the parent cloud on the evolution of the supercritical core, we compare four models (f , $m5$, $m7$ and $m9$). All have the same value of $n_{\text{opq}} = 10^{11} \text{ cm}^{-3}$, but an initial central mass-to-flux ratio (in units of the critical value for collapse) equal to 0.25, 0.5, 0.7 and 0.9, respectively. In Figures (10) and (11), model f is represented by a solid line, model $m5$ by a triple-dot-dashed line, model $m7$ by a dashed line, and model $m9$ by a dashed-dot line.

Figure (10a) shows the central mass-to-flux ratio in units of the critical value as a function of the central number density of neutrals. Although the initial mass-to-flux ratio is different in these models, *all memory of the initial conditions is lost after the formation of the supercritical core, and the increase of the central mass-to-flux ratio with density is practically identical in all models.* A very similar behavior is exhibited by the (z - and r -) components of the central magnetic field, shown as functions of central density in Figures 10c and 10d, respectively. The final values of B_z (and B_r) in all models differ by less than a factor of 2. This behavior is even more pronounced in the case of Δ_e , the attachment parameter of the electrons, which is shown as a function of the central number density of neutrals in Figure 10e. Δ_e starts out at the same value in all models ($\Delta_e = 1$, which corresponds to perfect attachment of the electrons to the field lines), and evolves in the same manner in all models. At the end of each run, by the time a central temperature of 1000 K is reached, its values in the four models are: 0.92 (model f), 0.94 (model $m5$), and 0.95 (models $m7$ and $m9$).

The quantity that *is* significantly affected by the initial mass-to-flux ratio is the time required for a particular central density to be reached (see Fig. 10b). The cloud spends most of the time in the early phase, until a supercritical core forms. Thereafter the contraction becomes dynamic (accelerated, but much slower than free fall).

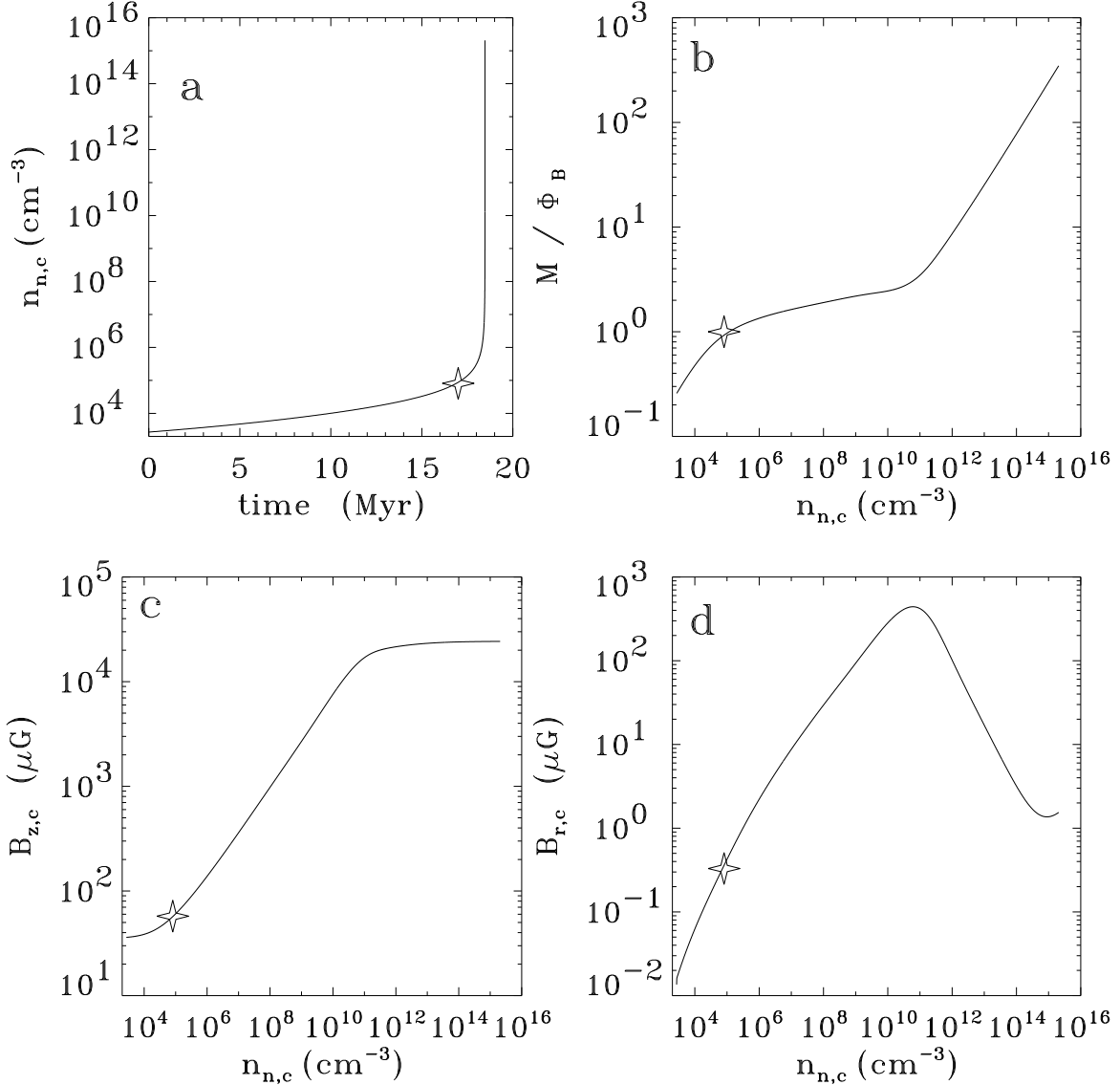


FIG. 7.— Evolution of central quantities for model *i* (isothermality assumption retained throughout the run). (a) Central number density of neutrals, normalized to its initial value in the reference state, as a function of time (in Myr); (b) mass-to-flux ratio, in units of the critical value, as a function of the central density enhancement; (c) z -component of the magnetic field, normalized to the field strength of the reference state, as a function of the central density enhancement; (d) r -component of the magnetic field, normalized to the field strength of the reference state, as a function of the central density enhancement. The “star” marks the formation of the supercritical core.

The total evolution time, from the initial state until the end of the run, ranges from 5 Myr (model *m9*) to 17 Myr (model *f*).

Figure (10f) shows the ratio of the ambipolar-diffusion and Ohmic-dissipation timescales at the center of the cloud, as a function of the central number density of neutral particles. Although the quantitative differences among models before the onset of adiabaticity are appreciable, the qualitative behavior is similar in all models. Models with smaller initial mass-to-flux ratio exhibit systematically smaller τ_{AD}/τ_{OD} values before the onset of adiabaticity. After adiabaticity sets in, the evolution of the timescales ratio is similar in all models. Ambipolar diffusion dominates Ohmic dissipation early on, but the two mechanisms become equally effective at central densities $\approx 10^{13} \text{ cm}^{-3}$ in all cases.

Figure (11) shows radial profiles of different quantities for models *f*, *m5*, *m7* and *m9*. All curves correspond

to that instant in time when the central number density of neutrals reaches the value $n_{n,c} = 10^{14} \text{ cm}^{-3}$. On each curve in these plots, the “star” marks the location of the boundary of the supercritical core in the corresponding model.

Figure (11a) shows the central number density of neutrals as a function of radius for each of the four models. At the late time corresponding to these curves, the established density profile is practically identical in all models, except near the boundary of the supercritical core, where small deviations between models can be identified. Just outside the boundary of the supercritical core, the density profile is steeper for smaller mass-to-flux ratios, because the envelopes are better supported by magnetic forces.

Figure (11b) shows the profiles of the z -component of the magnetic field for the four models. The field strength in the initial state of the parent cloud, which is preserved

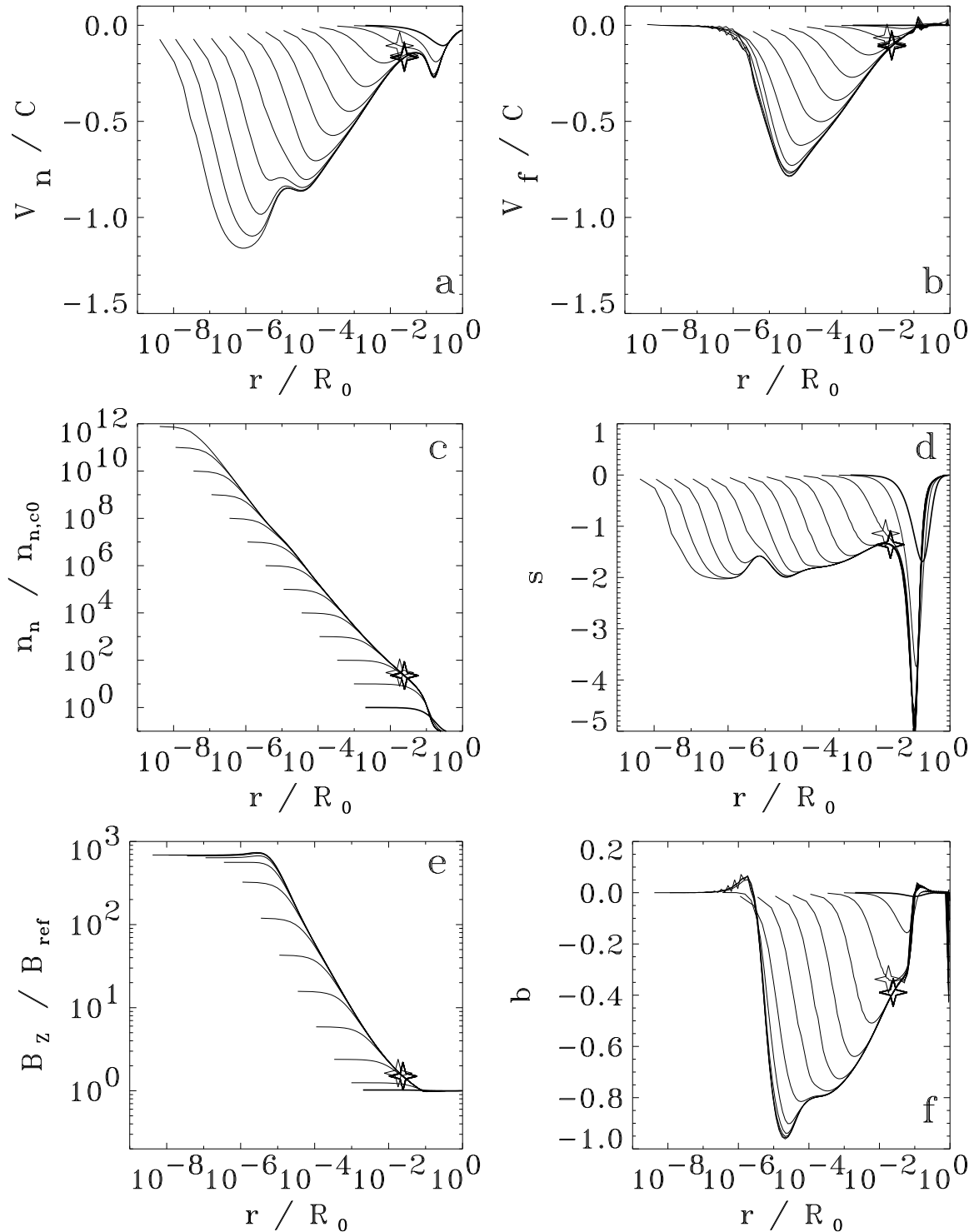


FIG. 8.— Spatial profiles of physical quantities of model *i* (isothermal run) at different times, chosen as in Figure (2). (a) Velocity of neutrals normalized to the sound speed of the reference state; (b) velocity of the field lines normalized to the sound speed of the reference state; (c) number density of the neutrals normalized to the initial central density of the reference state; (d) slope of the density profile $s = d \ln n_n / d \ln r$; (e) z -component of the magnetic field normalized to the field strength of the reference state; (f) slope of B_z , $b = d \ln B_z / d \ln r$. The “star” marks the location of the supercritical core boundary.

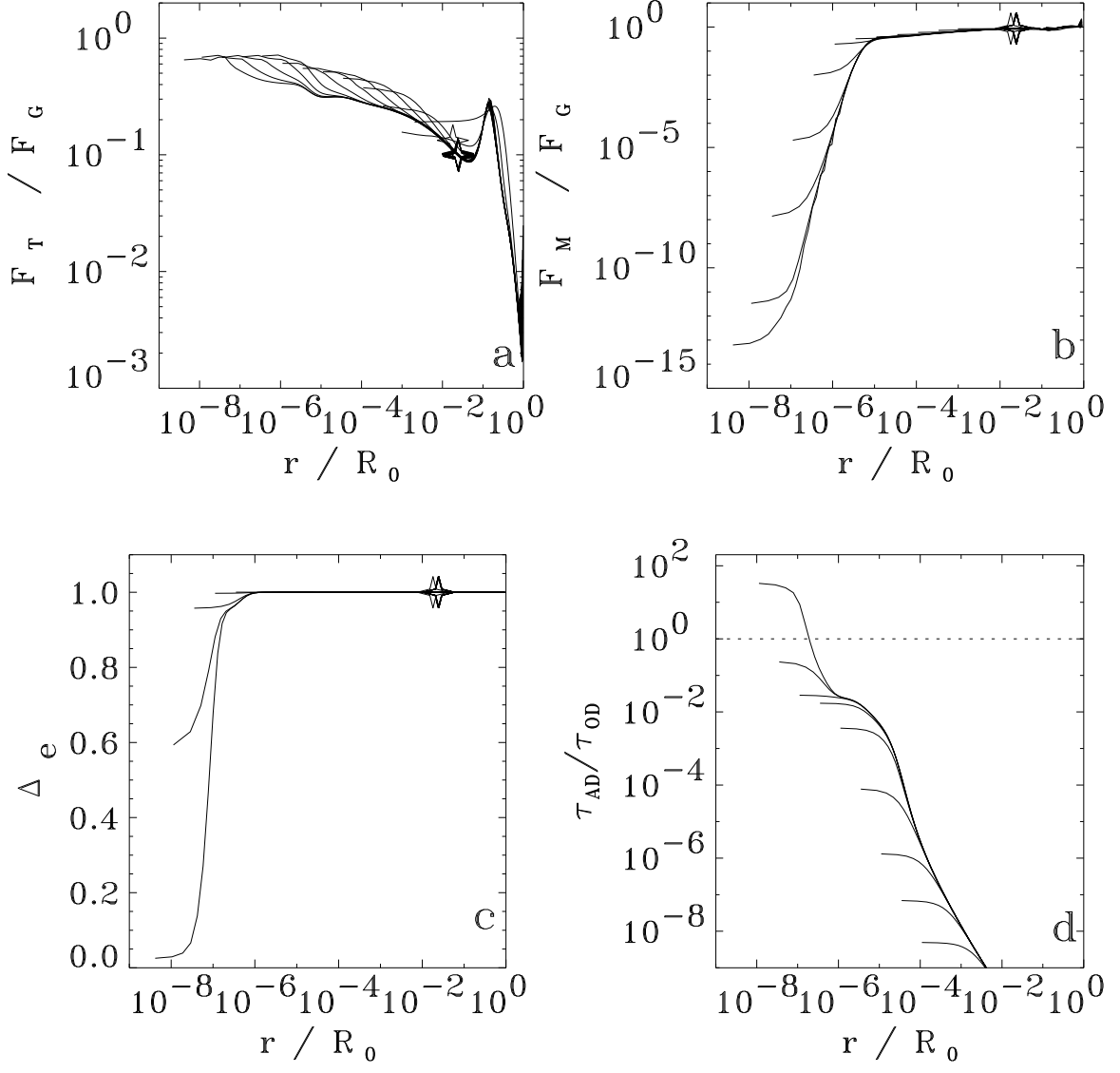


FIG. 9.— Radial profiles of physical quantities of model *i* (isothermal run) at different times, chosen as in Figure (2). (a) Ratio of thermal-pressure and gravitational forces; (b) ratio of magnetic and gravitational forces; (c) attachment parameter of electrons; (d) ratio of ambipolar-diffusion and Ohmic-dissipation timescales (the dotted line corresponds to $\tau_{AD} = \tau_{OD}$). The “star” marks the location of the supercritical core boundary.

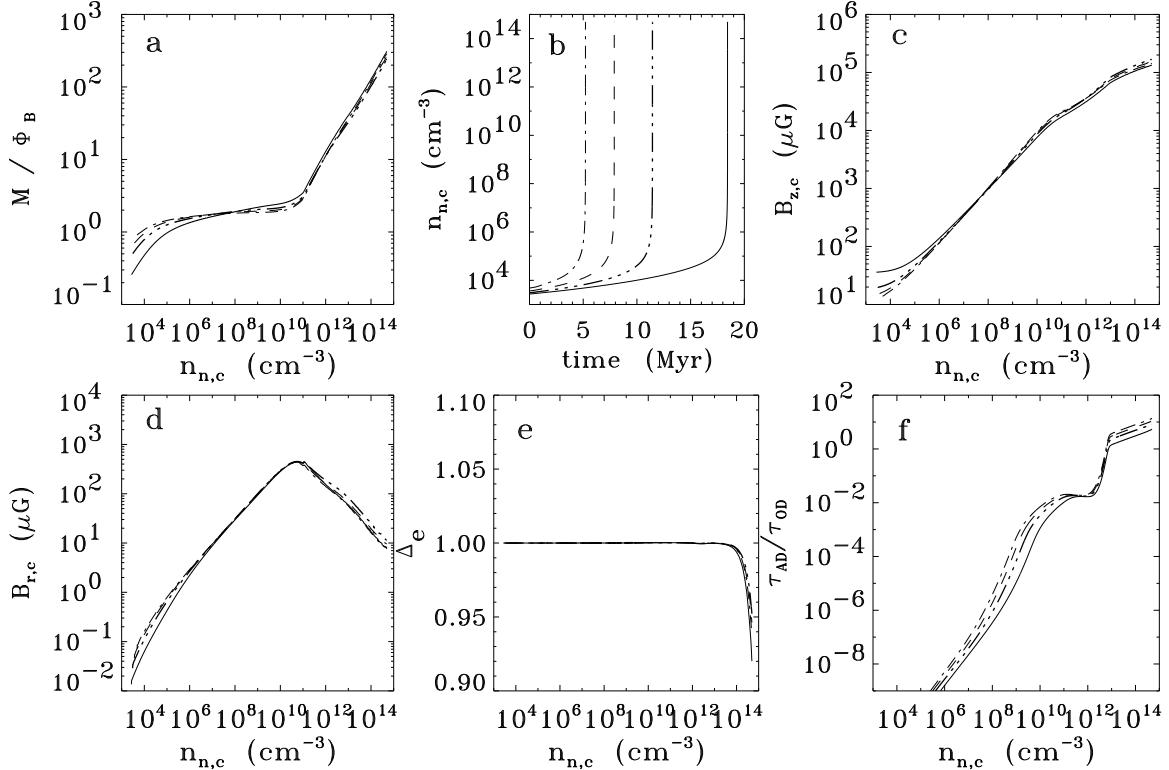


FIG. 10.— Evolution of central quantities for models *f* (solid line, $\mu_{d,c0} = 0.25$), *m5* (triple-dot-dashed line, $\mu_{d,c0} = 0.5$), *m7* (dashed line, $\mu_{d,c0} = 0.7$) and *m9* (dashed-dot line, $\mu_{d,c0} = 0.9$). (a) Central mass-to-flux ratio, normalized to the critical value, as a function of the central number density of neutrals; (b) central number density of neutrals as a function of time; (c) and (d) z - and r -components, respectively, of the magnetic field, as functions of neutral density; (e) attachment parameter of the electrons; (f) ratio of ambipolar-diffusion and Ohmic-dissipation timescales.

in the outermost regions of the model cloud, is different in each model, and is greater in models with smaller mass-to-flux ratio. However, within one order of magnitude in radius inward from the location of the supercritical core, the profile of B_z is almost the same in all models.

Figure (11c) shows profiles of the radial velocity of the neutral particles in units of the sound speed of the reference state. Although the behavior is qualitatively the same for all models, the evolution of the velocities and the values at their local minima depend on the initial mass-to-flux ratio. Inward of the location of the supercritical core boundary, the magnitude of the infall velocities achieved at a certain radius is greater for smaller initial mass-to-flux ratio. The reason for this trend is that the dynamical contraction sets in at a greater central density enhancement as the initial mass-to-flux ratio decreases. As a result, by any given central number density, the core will have spent less time in the dynamical phase in the models with smaller mass-to-flux ratio, and the resulting velocities will be smaller at any given radius. For this reason, the maximum infall velocity achieved by the neutrals increases as the initial mass-to-flux ratio increases, and is greatest in model *m9*.

Inward of the magnetic shock, the neutrals are reaccelerated by gravity before the thermal shock, behind which they almost come to rest in the hydrostatic core. The reacceleration is smaller for smaller initial mass-to-flux ratios because, as we have seen, the density profile is somewhat steeper at radii smaller than the radius at which adiabaticity sets in; hence, the thermal-pressure force is greater, presenting a greater opposition to grav-

ity.

This interpretation is verified by Figure (11e), which shows profiles of the ratio of thermal-pressure and gravitational forces in each model. The thermal-pressure force is indeed a greater fraction of the gravitational force in the reacceleration region (inward of the magnetic shock) in the models with smaller mass-to-flux ratios. The magnetic force, on the other hand, decreases rapidly with decreasing radius inward of the plateau of the magnetic force, where it balances gravity. In addition, the magnetic force as a fraction of the gravitational force has almost identical behavior in all models at a given value of the density. This can be seen clearly in Figure (11f), which plots the ratio of the magnetic and gravitational force in each model.

The profiles of the velocity of the field lines, v_f , in the four models are compared in Figure (11d). The velocity of the field lines exhibits only the magnetic-wall feature, because the deceleration at the magnetic shock brings them, as well as the attached species (the electrons), almost to rest. Hence the presence of the hydrostatic core boundary does not affect the motion of the field lines significantly. The maximum infall velocity exhibited by the field lines is greater in models with greater initial mass-to-flux ratios, because dynamical contraction operates for a longer time.

4. ^{26}Al AS AN ALTERNATIVE RADIONUCLIDE

All models discussed above assumed that, at very high densities, when the central part of the collapsing core becomes self-shielded from cosmic-ray ionization, the ion-

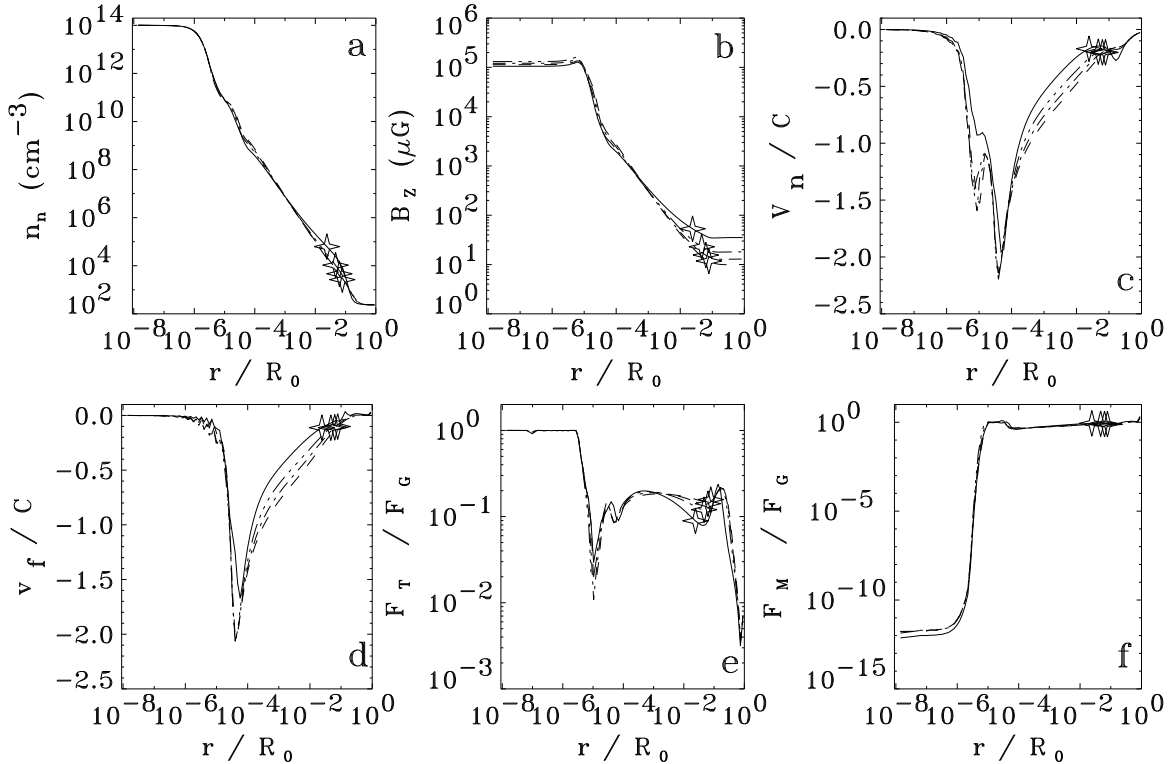


FIG. 11.— Radial profiles for models *f* (solid line), *m5* (triple-dot-dashed line), *m7* (dashed line) and *m9* (dashed-dot line), when the central density is $n_{n,c} = 10^{14} \text{ cm}^{-3}$. (a) Central density of neutrals; (b) z -component of the magnetic field; (c) radial velocity of neutrals; (d) radial velocity of magnetic field lines; (e) ratio of thermal-pressure and gravitational forces; (f) ratio of magnetic and gravitational forces. The “star” on each curve marks the location of the supercritical core boundary.

ization rate is dominated by ^{40}K radioactivity (half-life = 1.25 Gyr). If, however, the initial mass-to-flux ratio of the parent cloud is relatively close to critical, then the evolution is rapid and radionuclides with smaller lifetimes (such as ^{26}Al , with a half-life = 0.716 Myr) can dominate the ionization at high densities. Similarly, ^{26}Al can become important if the core happens to get enriched because of a nearby Supernova explosion. In this section we compare results from models *m9* and *Al*, both of which have an initial central mass-to-flux ratio equal to 0.9 times the critical value and $n_{\text{opq}} = 10^{11} \text{ cm}^{-3}$. Their difference lies in the radionuclide assumed to dominate high-density ionization, which is ^{40}K in model *m9* and ^{26}Al in model *Al*.

Figure (12) shows chemical abundances of different species as fractions of the number density of neutral hydrogen molecules (left column) and the ionization rate as a function of number density (right column) for models *m9* (top row) and *Al* (bottom row). In the case of model *Al*, the plateau reached by the ionization rate at high densities occurs at considerably greater values (more than three orders of magnitude) than in model *m9*. As a result, the degree of ionization and the chemical abundances of all charged species are significantly greater at high densities, when the ionization rate is dominated by radioactive decays.

The greater degree of ionization at high densities affects the degree of attachment of the electrons on the field lines. Figure (13) shows radial profiles of the indirect (Δ_e , left column) and direct ($\omega_e \tau_{\text{en}}$, right column) attachment parameters of the electrons, at different values of the central number density of the neutrals. The top-

row plots correspond to model *m9* and the bottom-row plots correspond to model *Al*. As we discussed in § 3, the attachment parameter in model *m9* remains very close to 1 throughout the run, and hence the electrons are always well coupled to the magnetic field. However, in model *Al* at high densities, the attachment parameter of the electrons falls below 0.8, and hence the electrons have started to detach by the end of the run. This effect is clearly not of magnetic origin, since the magnetic field (and the direct attachment parameter of the electrons at a given density) is essentially the same in the two models. Instead, the effect is electrostatic: the increased abundance of positively-charged species (positively-charged grains and ions), all of which have completely detached from the field lines and are following the motion of the neutrals by the densities of interest, exerts attractive electrostatic forces on the electrons, which thereby begin to detach earlier than they otherwise would.

A second important effect of the higher degree of ionization in model *Al* is the difference in the dependence on number density of the ratio of the ambipolar-diffusion and Ohmic-dissipation timescales, which can be seen in Figure (14). The increased degree of ionization and the better attachment of electrons to field lines allowed ambipolar diffusion to operate for higher densities and hence its timescale to remain smaller than that of Ohmic dissipation throughout the run.

5. CONCLUSIONS AND DISCUSSION

In Paper II, we presented results for the ambipolar-diffusion-initiated formation and contraction of a protostellar fragment inside a self-gravitating, magnetically

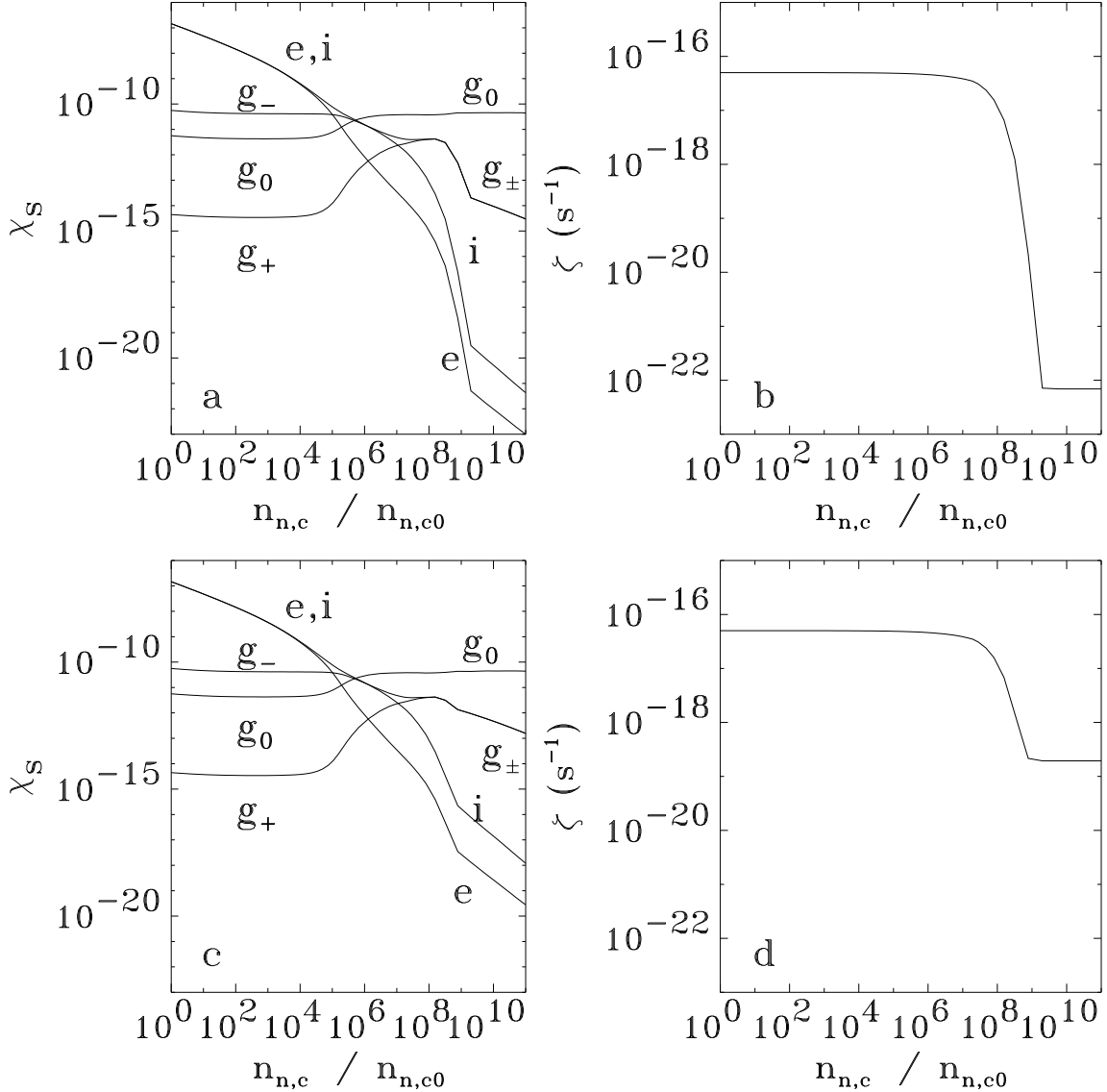


FIG. 12.— Abundances of different species (left column) and ionization rate (right column) as functions of the central neutral density normalized to its initial value ($n_{n,c0} = 4900 \text{ cm}^{-3}$). *Top row*: model *m9* (^{40}K is the dominant radionuclide); *bottom row*: model *A1* (^{26}Al is the dominant radionuclide).

supported model molecular cloud, with a fiducial set of values for the free parameters. We followed the evolution of the fragment into the opaque regime, through the formation of a hydrostatic protostellar core and the later onset of thermal ionization. In this paper, we assessed the sensitivity of the solution on the values of the free parameters; namely, the density of neutrals n_{opq} above which the equation of state becomes adiabatic, the initial central mass-to-flux ratio $\mu_{d,c0}$ of the parent cloud (relative to its critical value for collapse), and the radionuclide that dominates the ionization at the highest densities ($n_n \gtrsim 10^{12} \text{ cm}^{-3}$).

We found that varying n_{opq} did not result in any qualitatively or quantitatively significant change in the structure of the magnetic field inside the hydrostatic core. The value of $B_z \approx 0.1 \text{ G}$ reached by the end of each run (when $T = 1000 \text{ K}$) is almost the same in all cases and, remarkably, very close to the values of the protosolar magnetic field as measured in me-

teorites (Levy 1988; Stacey, Lovering, & Parry 1961; Herndon & Rowe 1974). The detachment of the electrons from the magnetic field lines (signifying the decoupling of the magnetic field from the matter) was found to occur at $n_n \approx 10^{15} \text{ cm}^{-3}$, provided that this density could be reached in the central part of the hydrostatic core before the temperature reached 1000 K. If the temperature of 1000 K is reached before the electrons have detached from the field lines, thermal ionization will recouple the field lines and the matter; hence, complete decoupling will never be achieved. This latter case was found to be the most likely outcome, because the electrons did not detach from the field lines unless adiabaticity set in only at very high neutral densities ($\gtrsim 10^{12} \text{ cm}^{-3}$). However, a detailed radiative transfer treatment is needed in order to follow the evolution of the core temperature more accurately and thereby arrive at a definitive conclusion concerning the decoupling of the magnetic field from the matter.

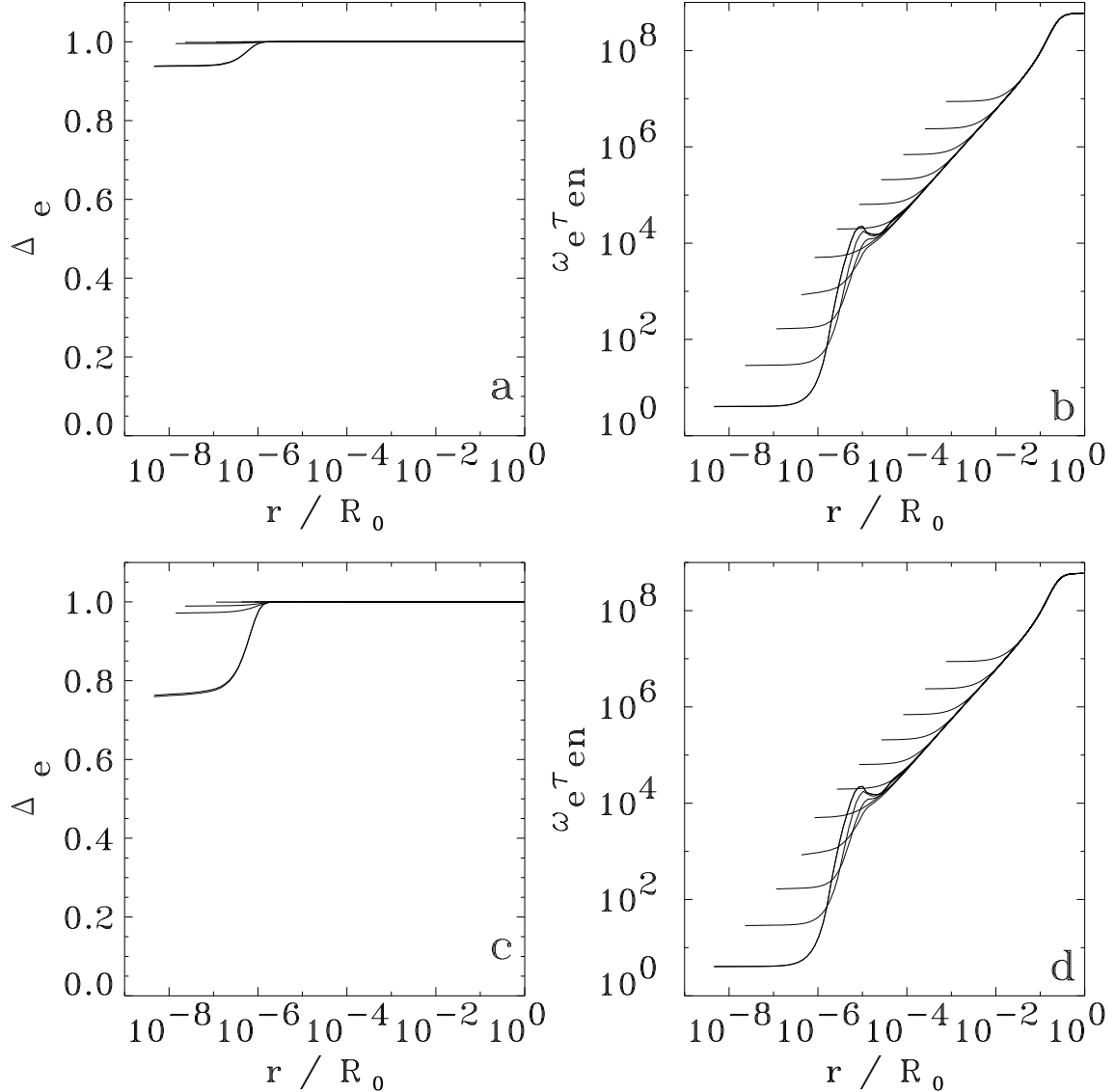


Figure 3. The structure of the magnetic field, the density at which the electron detachment takes place, and the relative importance of ambipolar diffusion and Ohmic dissipation in reducing the protostellar magnetic flux are insensitive to the assumed equation of state is also corroborated by the control isothermal run (in which the equation of state is assumed to remain isothermal throughout the core and for the entire duration of the run). However, the onset of adiabaticity and the formation of a central hydrostatic core did facilitate the development of the magnetic shock, which, in the adiabatic cases, formed at earlier times and was significantly stronger.

The effect of varying the initial mass-to-flux ratio of the parent cloud was found to be limited to the time required for the formation of the magnetically supercritical core (which is longer for the more subcritical clouds). Beyond that point, the supercritical core loses memory of the initial mass-to-flux ratio of the cloud, and the late-time results are qualitatively and quantitatively similar in all cases.

Finally, changing the dominant radionuclide (from ^{40}K to ^{26}Al) responsible for ionization at the late stages of the evolution, ($n_n \gtrsim 10^{12} \text{ cm}^{-3}$) led to the electrons beginning to detach from the magnetic field lines at slightly smaller densities, because the more abundant, detached, infalling positive charges enhanced the electrostatic attraction of the electrons. In addition, ambipolar diffusion remained more effective than Ohmic dissipation in reducing the magnetic flux of the protostellar core throughout the run.

KT would like to thank Vasiliki Pavlidou for useful discussions and Glenn Ciolek for providing the base version of the code used in this work. The work of KT was supported in part by the University of Illinois through a Dissertation Completion Fellowship. This research was partially supported by a grant from the American Astronomical Society and NSF grants AST 02-06216 and AST 02-39759.

REFERENCES

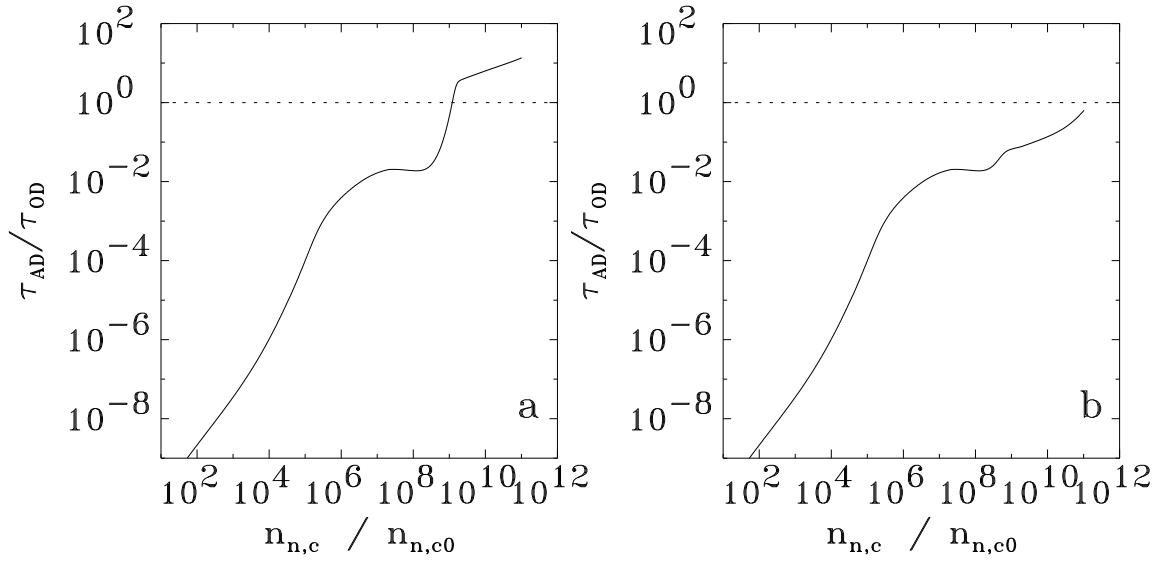


FIG. 14.— Ratio of ambipolar-diffusion and Ohmic-dissipation timescales in models *m9* (left) and *Al* (right) as a function of the central density normalized to its initial value ($n_{n,c0} = 4900 \text{ cm}^{-3}$).

Draine, B. T. & Lee, H. M. 1984, *ApJ*, 285, 89
 Gaustad, J. E. 1963, *ApJ*, 138, 1050
 Hayashi, C. 1966, *ARA&A*, 4, 171
 Herndon, J. M. & Rowe, M. W. 1974, *Meteoritics*, 9, 289
 Levy, E. H. 1988, in *Meteorites and the Early Solar System*, ed. J. F. Kerridge & M. S. Matthews (Tucson: Univ. Arizona Press)
 Masunaga, H. & Inutsuka, S. 1999, *ApJ*, 510, 822

Ossenkopf, V. & Henning, T. 1994, *A&A*, 291, 943
 Stacey, F. D., Lovering, J. F., & Parry, L. G. 1961, *J. Geophys. Res.*, 66, 1523
 Tassis, K. & Mouschovias, T. Ch. 2006a [paper I]
 —. 2006b [paper II]